Sensors and Actuators A 188 (2012) 148–157

Contents lists available at SciVerse ScienceDirect

Sensors and Actuators A: Physical

journal homepage: www.elsevier.com/locate/sna

Wide-bandwidth, meandering vibration energy harvester with distributed circuit board inertial mass☆

D.F. Berdy[a,c,*], B. Jung[a], J.F. Rhoads[b,c], D. Peroulis[a,b,c]

[a] School of Electrical and Computer Engineering, Purdue University, West Lafayette, IN 47907, USA
[b] School of Mechanical Engineering, Purdue University, West Lafayette, IN 47907, USA
[c] Birck Nanotechnology Center, Purdue University, West Lafayette, IN 47907, USA

ARTICLE INFO

Article history:
Received 31 August 2011
Received in revised form 24 January 2012
Accepted 26 January 2012
Available online 4 February 2012

Keywords:
Piezoelectric
Vibration
Energy harvesting
Wide bandwidth
Increased bandwidth
Sensor node

ABSTRACT

A wide-bandwidth, meandering piezoelectric vibration energy harvester is presented for the first time utilizing the sensor node electronics as a distributed inertial mass. The energy harvester achieves an experimental maximum power output of 198 μW when excited with a peak acceleration of 0.2 g (where 1 g is 9.8 m/s^2) at 35 Hz. The output power remains higher than half of the maximum power (99 μW) for the frequency band from 34.4 to 42 Hz, achieving a half-power fractional bandwidth of 19.9%, an increase of 4× compared to typical single-mode energy harvesters. The output power remains above 20 μW from 29.5 to 48 Hz, achieving a 20-μW fractional bandwidth of 48%. This is the highest reported fractional bandwidth for this low 0.2 g acceleration level. The distributed inertial mass in combination with the meandering harvester's close natural frequency spacing is what enables the wide bandwidth. The energy harvester is demonstrated to autonomously operate a sensor node to sense and transmit temperature through a 434 MHz on–off-keying wireless transmitter while the electronics are used as the inertial distributed mass.

1. Introduction

A primary constraint of modern day wireless sensor nodes is the lifetime limitation imposed by the use of primary batteries [1]. Unless the battery is a secondary battery, which has an external source of energy replenishing it, this fundamental lifetime limitation will always be an obstacle, thus increasing maintenance costs and down time due to battery replacement. To address this problem, researchers have proposed energy harvesting technologies to extract ambient energy from the environment to recharge batteries *in situ* or even entirely power the sensor node without the use of a battery [2]. The relatively low power requirements of modern sensor node circuitry makes energy harvesters a compatible and effective source for sensor nodes. Among ambient energy sources (solar, thermal, wind, vibration, etc.), mechanical vibration energy has gained significant attention recently due to its abundance in and around operating machinery, making it an effective source for powering structural health monitoring sensor nodes [3–6].

Vibration energy harvesters are commonly single-mode resonant systems with relatively narrow bandwidth set by the quality factor [7]. Therefore, the resonant frequency of the harvester must be designed to closely match the ambient vibration frequency to effectively extract energy. If the source vibration frequency and device resonant frequency are mismatched, power output is significantly reduced [8]. Frequency mismatch can occur due to manufacturing tolerance (i.e. process variation), source frequency variation, or energy harvester resonant frequency change due to aging [9]. The issues of frequency mismatch and narrow bandwidth are two of the most significant problems in vibration energy harvesting because each device is highly application specific and susceptible to changes in ambient conditions [7].

An important metric to characterize a vibration energy harvester's tolerance to frequency deviations is fractional bandwidth (FBW), which is defined as the bandwidth of the energy harvester divided by its center frequency. A typical linear single-mode resonant energy harvester with quality factor of 20 [8] has a FBW of 5%. The FBW versus acceleration has been plotted in Fig. 1 for several energy harvesting devices reported in literature [10–50]. As seen in the figure, the fractional bandwidths range from less than 1% up to 53%. The two devices with the highest fractional bandwidths (53% [10] and 20% [29]) are both electromagnetic energy harvesters that utilize nonlinear phenomena to achieve a high fractional bandwidth. A drawback of the nonlinear approaches in literature is that the base excitation level must be relatively large to achieve the large

☆ TRANSDUCERS XVI (2011) Paper #: **W3P.167**.

* Corresponding author at: School of Electrical and Computer Engineering, Purdue University, West Lafayette, IN 47907, USA. Tel.: +1 765 4968374.
E-mail addresses: david.berdy@ieee.org (D.F. Berdy), dperouli@purdue.edu (D. Peroulis).

0924-4247/$ – see front matter © 2012 Elsevier B.V. All rights reserved.
doi:10.1016/j.sna.2012.01.043

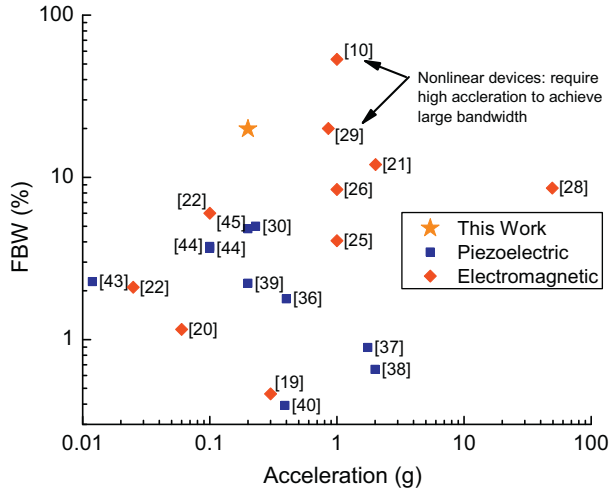

Fig. 1. Summary of fractional bandwidths for energy harvesters from literature.

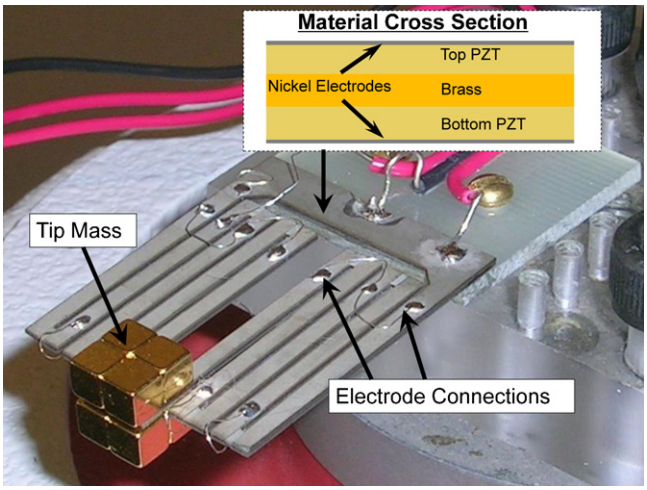

Fig. 2. Meandering energy harvester showing material cross section.

deflections that enable bandwidth widening. For example, in [10], the excitation acceleration was 1 g (where 1 g is equal to 9.8 m/s^2), which is higher than many ambient vibration source amplitudes [51].

In this paper, we expand on the recent increased-bandwidth meandering energy harvester presented by the authors [52]. For the first time, the energy harvester utilizes the sensor node electronics as a distributed inertial mass. The sensor electronics autonomously operate from the energy provided by the harvester. The distributed mass in combination with the meandering energy harvester's unique mode shapes are exploited to increase the fractional bandwidth (FBW) to 19.9%, which is a 4× increase compared with typical single mode devices. This is believed to be the highest reported FBW for a piezoelectric energy harvester and the highest FBW for an energy harvester operating at 0.2 g. The results of this paper show the potential of utilizing the electronics as a distributed mass in order to achieve a wide bandwidth.

The target application of the proposed energy harvester and sensor node is structural condition monitoring. Vibration environments for this application typically have peak acceleration magnitude at frequencies lower than 100 Hz with acceleration magnitude typically less than 0.5 g [51]. As an example, a car driven at 65 mph has a peak vibration acceleration of about 0.15 g at 35 Hz [53] and a helicopter exhibits structural resonances at frequencies of 20 and 40 Hz [54]. The target operating frequency of the device in this paper is 40 Hz at an acceleration magnitude of 0.2 g.

The paper is organized as follows. Section 2.1 describes the operating principle of the meandering energy harvester with the distributed inertial mass. Section 2.2 uses finite element analysis to predict the performance of the energy harvester. A wireless sensor node circuit is presented in Section 2.3. The experimental results are presented and discussed in Section 3 and the paper is concluded in Section 4.

2. Design

2.1. Meandering energy harvester with circuit board inertial mass

The energy harvester used in this work is based on the low frequency meandering piezoelectric vibration energy harvester previously presented by the authors and shown in Fig. 2 [39]. The device is a double-clamped cantilevered piezoelectric bimorph that has been meandered, or bent into a serpentine-like shape, in order to reduced the device length. The cross section consists of a piezoelectric bimorph beam with central brass shim, top and bottom piezoelectric layers of lead zirconate titanate (PZT), and thin nickel electrodes. The tip mass added to the end of the device further reduces resonant frequency while increasing power output.

The meandering energy harvester was fabricated by cutting commercial bimorph material from Piezo Systems (T226-A4-503Y) using a femtosecond pulsed laser [39]. Due to the meander's unique shape, both positive and negative strains are present in the piezoelectric layer at the first and second vibration modes, which would tend to cause voltage cancellation if a single electrode covered the device, as described later in this section. Therefore to avoid voltage cancellation, the electrodes were cut using laser ablation at strain nodes to separate regions of positive and negative strain [55]. The positive and negative electrode segments were connected together using thin wires [39].

The main advantage of the meandering shape compared to a comparably sized straight cantilever energy harvester is a 70% reduction in resonant frequency for the device in Fig. 2. An additional advantage of the meander is that the natural frequencies are more closely spaced, reducing first and second mode spacing by 5 times compared with the straight cantilever [56]. These results indicate that the meander is well-suited for multi-modal, increased-bandwidth vibration energy harvesting.

The initial design for the approximate dimensions of the meandering energy harvester shown in Fig. 2 was accomplished using lumped-element modeling followed by fine tuning in finite element analysis (FEA) software (ANSYS). The overall footprint of approximately 23 mm × 23 mm was chosen for our application. The design procedure was to model the structure as two N-segment springs supporting a tip mass (as shown in Fig. 2). Assuming the individual segments of the meander act as springs and the connection points between segments are rigid, the effective spring constant (k_{eff}) of the device can be approximated using series and parallel spring combinations as

$$k_{eff} = 2\frac{k_{cantilever}}{N} \quad (1)$$

where $k_{cantilever}$ is the spring constant of the individual cantilever segment and N is the number of segments of the two springs supporting the tip mass (N = 5 in Fig. 2). Each section is modeled as a cantilever beam with a spring constant of

$$k_{cantilever} = \frac{3EI}{L^3} \quad (2)$$

where EI is the flexural rigidity of the composite bimorph and L is the length of the beam segment. The flexural rigidity of the multilayer beam can be calculated by:

$$EI = \frac{2wt_p^3E_p}{3}\left[\frac{E_s t_s^3}{E_p 8t_p^3} + \frac{3t_s^2}{4t_p^2} + \frac{3t_s}{2t_p} + 1\right] \quad (3)$$

where w is the beam width, t_p and t_s are the piezoelectric layer and center shim thickness, respectively, and E_p and E_s are the piezoelectric layer and center shim elastic modulus [57]. Finally the resonant frequency of the beam is estimated by

$$\omega = \sqrt{\frac{k_{eff}}{m_{eff}}} = \sqrt{\frac{k_{eff}}{M_t}} \quad (4)$$

where M_t is the tip mass [58]. Note that the effective mass of the structure could be incorporated here in addition to the tip mass to improve model fidelity. Using these equations, a meander was designed with $N = 5$, $L = 23$ mm, and $w = 1.5$ mm with a tip mass of 1.92 g to achieve a resonant frequency of 55.6 Hz. The resonant frequency of this design was found to be 49.5 Hz in ANSYS.

Unlike the previous work [39], the current study implements, for the first time, a distributed inertial mass to push the first two natural frequencies of the meander closer together to achieve a much wider bandwidth. A unique added benefit of this approach is that the distributed mass can be composed of the sensor node electronics and circuit board, potentially leading to a more compact system. A diagram of the sensor node with meandering energy harvester and distributed mass is shown in Fig. 3. The sensor node consists of the circuit board and components, an additional overhang mass, the central attachment point mass, and the meandering energy harvester. The additional overhang mass is used if the circuit board does not have enough mass to achieve the required resonant frequency or output power.

The simulated first two mode shapes of the meander with distributed mass are shown in Fig. 4. The figure illustrates the peak vertical displacement in relation to the structure at rest as well as the strain contour at the surface of the piezoelectric. In mode A, the structure deflects with maximum displacement at the tip of the meander, while mode B deflects with maximum displacement at the center meander section closest to the anchor. The overhanging distributed mass and circuit board have minimal deformation and strain due to their relatively large thickness. This is desirable because only strain energy in the piezoelectric sections is converted to electrical energy.

The mode shapes of Fig. 4 show that regions of both positive and negative strain exist in the piezoelectric layer. Based on the piezoelectric effect, the open circuit voltage generated is proportional to strain [59]. Therefore, if regions with both positive and negative strain were covered by a single electrode the positive and negative voltages would cancel. To avoid the voltage cancellation issue, two separate electrodes must be used to cover the regions of positive and negative strain [39].

The first two modes of the meandering energy harvester with distributed inertial mass can approximately be modeled as a two-degree-of-freedom (2-DOF) spring-mass-dashpot system in which the natural frequencies are found by

$$f_x = \frac{1}{2\pi}\sqrt{\frac{k_x}{m_x}} \quad (5)$$

where k_x and m_x are the effective spring constant and modal mass, respectively, and x is the subscript denoting the mode (A or B). In Fig. 3, the central mass location is defined by the distance, L_{CM}, from the central mass edge to the meander edge closest to the anchor point. As L_{CM} is increased (i.e. the central mass moves from left to right in the side view of Fig. 3), f_A decreases while f_B increases. Accordingly, the relative frequencies of mode A and mode B can be shifted closer or further from each other by adjusting L_{CM}. In the next section, this is verified via simulation.

Table 1
Material properties and simulation parameters [62].

Piezoelectric properties	
Relative dielectric constant (ε_r)	1800
33 Piezoelectric strain coefficient (d_{33})	390×10^{-12} m/V
31 Piezoelectric strain coefficient (d_{31})	-190×10^{-12} m/V
Piezoelectric density (ρ_p)	7800 kg/m^3
Elastic modulus (Y_3^E)	5.2×10^{10} N/m^2
Elastic modulus (Y_1^E)	6.6×10^{10} N/m^2
Piezo electric thickness (t_p)	0.25 mm
Shim and mass properties	
Shim density (ρ_s)	8500 kg/m^3
Shim elastic modulus (E_s)	10×10^{10} N/m^2
Center shim thickness (t_s)	0.11 mm
Center mass elastic modulus ($E_c m$)	10×10^{10} N/m^2
Center mass density (ρ_{cm})	5400 kg/m^3
Circuit board elastic modulus (E_{FR4})	2×10^{10} N/m^2
Circuit board density (ρ_{FR4})	2400 kg/m^3
Circuit component density (ρ_{ckt})	850 kg/m^3
Antenna density (ρ_{ant})	2700 kg/m^3
Other parameters	
Acceleration magnitude ($A_{(peak)}$)	0.2 g
Width of meander segments (w_{meand})	1.5 mm
Spacing between meander segments (w_{sp})	0.5 mm
Damping coefficient (ζ)	0.022

One thing that should be noted is that when $L_{CM} = 0$, there is no strain in the central two beams of the meander. This is because when the central mass is placed closest to the anchor, there is no inertial mass forcing the central beam sections to bend and therefore no useful power output is extracted from these sections. However, as the central mass moves away from the anchor (L_{CM} increases) bending strain is induced in the central beam sections and these sections produce a useful amount of power.

2.2. Finite element analysis

The finite element analysis package ANSYS [60] is used to demonstrate the operation of the device at its first two resonant modes and predict its performance. The energy harvester is modeled in ANSYS as being connected directly to a load resistor to extract the root mean square (RMS) output power of the energy harvester [36]. In the simulation, the energy harvester is excited by an imposed displacement vibration amplitude of 0.2 g by applying a harmonic vertical displacement on the anchor point nodes of

$$|Y| = \frac{A_{(peak)}}{(2\pi f)^2} \quad (6)$$

where Y is the imposed base displacement amplitude, $A_{(peak)}$ is the peak imposed acceleration amplitude and f is the frequency of excitation [61]. The material properties and other parameters used in simulation are shown in Table 1 [62].

The dimensions of the meandering energy harvester and attached masses are shown in Fig. 3. The dimensions of the energy harvester are based on the single point-mass energy harvester shown in Fig. 2 and discussed in Section 2.1. The overhang circuit board dimensions were determined by the number and size of components required for the sensor node circuitry, which was found to be 27.5 mm by 27.5 mm for the prototype circuit that is discussed in Section 2.3. The size of the additional overhang mass beneath the circuit board was decided by the circuit board dimensions and the area required for the antenna ground clearance. Typically required for small chip or printed circuit board antennas, ground clearance refers to the area around the antenna that must be clear of metals, such as circuit board metal or the overhang mass metal. In this case the maximum overhang mass length is 20 mm. The thickness of the

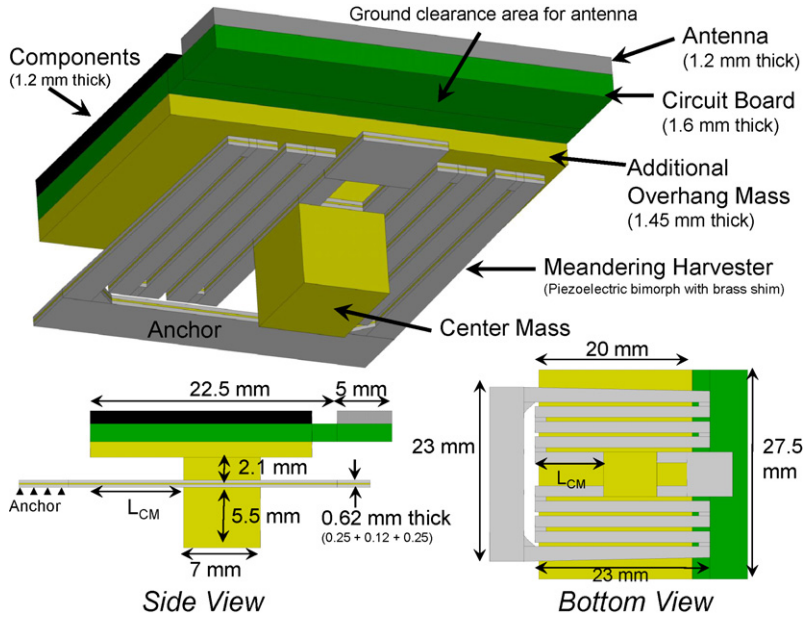

Fig. 3. Sensor node including meandering energy harvester with distributed circuit board mass.

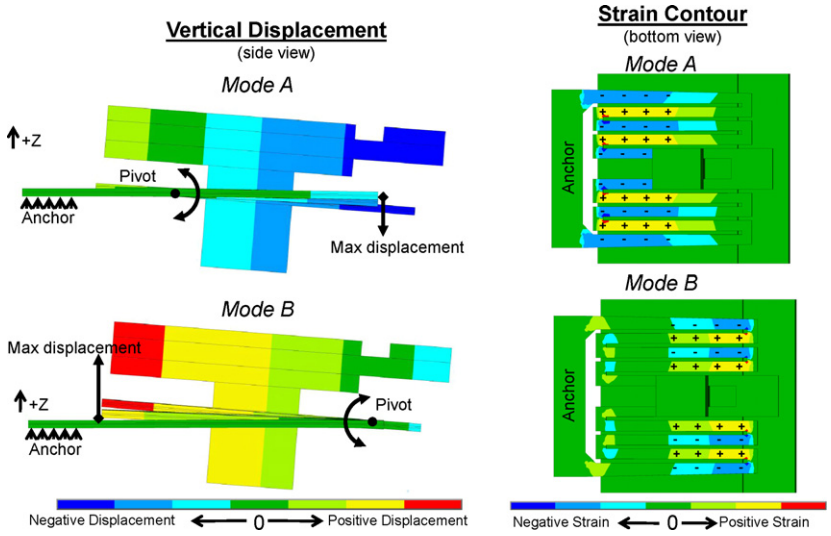

Fig. 4. Simulated mode shapes (mode A and mode B) of the first two mode shapes of the meander with overhanging mass (simulated in ANSYS).

additional mass below the circuit board was adjusted in simulation to achieve a center frequency close to 40 Hz.

Since the dimensions of the energy harvester, mass, and circuit board have been fixed, the last design choice is where to place the central mass for optimal bandwidth. The placement of the central mass can be used to set the spacing between the first and second mode frequencies. By controlling the location of the center mass (L_{CM}), the modal masses and stiffnesses of modes A and B can be adjusted.

The location of the central mass was varied in the simulation to predict where the mass should be placed for optimal bandwidth. A plot of the modal frequencies extracted from ANSYS is shown in Fig. 5 versus L_{CM}. The simulation results verify that as L_{CM} increases, the frequency of mode A decreases, while the frequency of mode B increases, thus allowing control of the spacing between mode A and mode B. The simulated RMS power across a 400 kΩ load is shown in Fig. 6 for values of L_{CM} ranging from 3 to 12 mm. The simulation results show a peak power of 251 μW at a frequency of 32.25 Hz and optimal half-power bandwidth of 5.5 Hz for

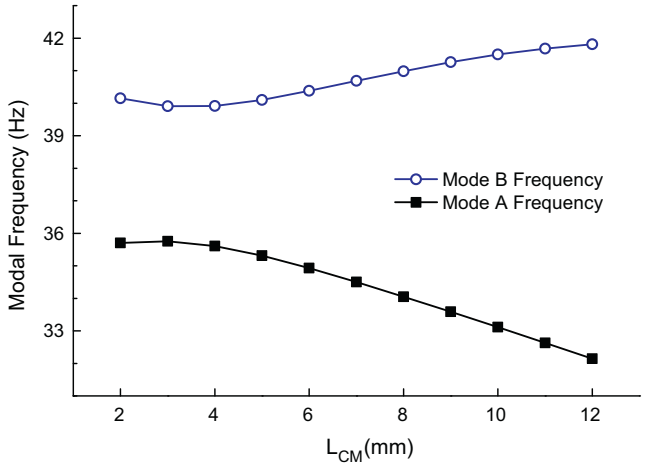

Fig. 5. Simulated modal frequencies as a function of central mass placement (L_{CM}).

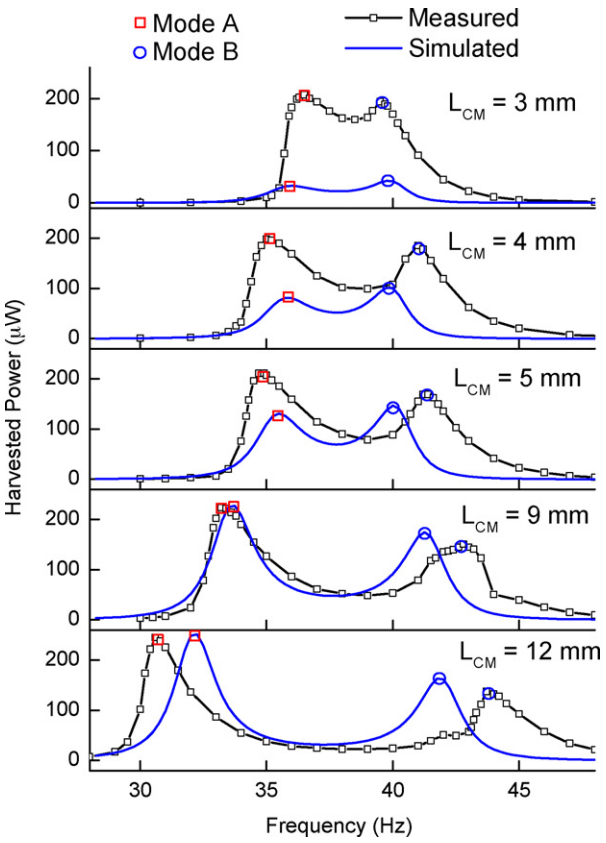

Fig. 6. Simulated and measured RMS harvested power across a 400 kΩ resistor as a function of frequency for different values of L_{CM} at an acceleration magnitude of 0.2 g.

L_{CM} = 4 mm. The simulation results also predict that as the modes become more closely spaced, the peak power output decreases. These results will be compared to the measurement results and discussed further in Section 3.2.

2.3. Sensor node circuitry

In order to test and demonstrate the concept of utilizing the sensor node circuitry as an overhanging distributed mass for energy harvesting, a wireless sensor node circuit was developed using commercial components. The block diagram of the circuit is shown in Fig. 7 and has a structure similar to the circuit used in [63]. The AC voltage from the energy harvester is rectified and stored in a 47 μF ceramic capacitor acting as an energy reservoir. A ceramic capacitor is chosen due to the low leakage when compared to other capacitor types [64]. The energy in the rectifier capacitor ($E_{Rect} = C_{Rect}V^2/2$) must be large enough to supply the energy during the transmit cycle ($E_{tx} = P_{tx}t_{tx}$), thus the minimum capacitance value is determined by solving for C_{Rect} in $E_{Rect} = E_{tx}$ to get:

$$C_{Rect} = \frac{2P_{tx}t_{tx}}{V_{high}^2 - V_{low}^2} \tag{7}$$

where P_{tx} is the power consumption during transmission, t_{tx} is the desired transmit time, V_{high} and V_{low} are the upper and lower voltage thresholds on the rectifier capacitor. V_{high} is set to 6.1 V, which is chosen to be lower than the open circuit rectified voltage of the energy harvester at the frequency range of interest to ensure the energy harvester can reach the upper threshold level. V_{low} is set to 3.2 V, which is slightly above the regulator output voltage. The threshold voltages are set by a Schmitt trigger implemented with a micro-power comparator (LTC1540). When the Schmitt trigger detects that the capacitor voltage is above V_{high}, a switching regulator (TPS62120) is enabled to provide a 3 V supply for the sensor interface and RF transmitter. The transmitter current consumption is 5.7 mA based on the transmitter datasheet, thus during transmit, the power consumption is about 34.8 mW (5.7 mA at 6.1 V) [65]. The transmission time was chosen to be 10 ms to allow adequate time to ensure the regulator and transmitter have sufficient time to stabilize. Based on Eq. 7, the required capacitance value is 26 μF, however, the most readily available standard capacitance value was 47 μF.

The sensor implemented is a thermistor to measure temperature. The resistance of the thermistor controls the frequency of an oscillator based on a 555 timer. The frequency of the signal at the output of the oscillator is [63]

$$f_{osc} = \frac{1.44}{(R_1 + 2R_{Therm})C_1}. \tag{8}$$

The oscillator output signal is fed into a wireless RF transmitter (MAX1472) operating at 434 MHz. The transmitter uses on–off keying (OOK) to modulate the variable-frequency signal onto the 434 MHz RF carrier. In order to minimize the size of the sensor node circuitry, a chip antenna (Johanson Technologies 0433AT62A0020) is used in the transmitter at the cost of reduced efficiency due to a relatively small ground plane.

3. Results

3.1. Stand alone circuit test

Measurements of the circuit in Fig. 7 without the energy harvester attached were completed first to validate the circuit operation. At a rectified voltage of 6 V, the circuit consumed 10.4 μW while the linear regulator was disabled (i.e. in the harvesting stage) and at 6.6 V, during transmission, the power consumption was 37.6 mW. After initial validation, the circuit was placed in a thermal oven to record the sensor interface output frequency as a function of temperature. The result of the theoretical and measured values of the sensor interface output frequency are shown in Fig. 8. The measured frequency follows the model results based on the thermistor datasheet values with some minor deviation due to neglecting the effect of temperature on components other than the thermistor.

3.2. Stand alone energy harvester test

A picture of the fabricated device and experimental setup are shown in Figs. 9 and 10, respectively. The meandering energy harvester with overhanging circuit mass was mounted on an electrodynamic shaker (TIRA TV51120) with accelerometer (Crossbow CXL04GP1Z) to measure the applied acceleration. Thin flexible wires were attached to the circuit board to measure the voltage supply lines and sensor interface signal during operation with minimal disturbance to the harvester vibration. A thermocouple (TME Type K) was placed close to the harvester to measure the ambient temperature around the sensor node. The receiving antenna (Linx Tech. Inc. ANT-433-CW-RH) was placed approximately 0.4 m away from the sensor node and the received signal was captured on a high speed oscilloscope (Tektronix DPO7104) to view the RF signal.

The measured RMS harvested power across a 400 kΩ load resistor is shown in Fig. 6 for various central mass positions. The minimum value of L_{CM} that could be achieved experimentally was 3 mm due to the electrode connection wires that were soldered to the piezoelectric layer from L_{CM} = 0 mm to L_{CM} = 3 mm as described in Section 2.1. The load resistance was swept to find an optimal value of 400 kΩ for maximum power output.

In the measurement results, the half-power bandwidth is maximized when L_{CM} = 4 mm. Higher values of L_{CM} have power output

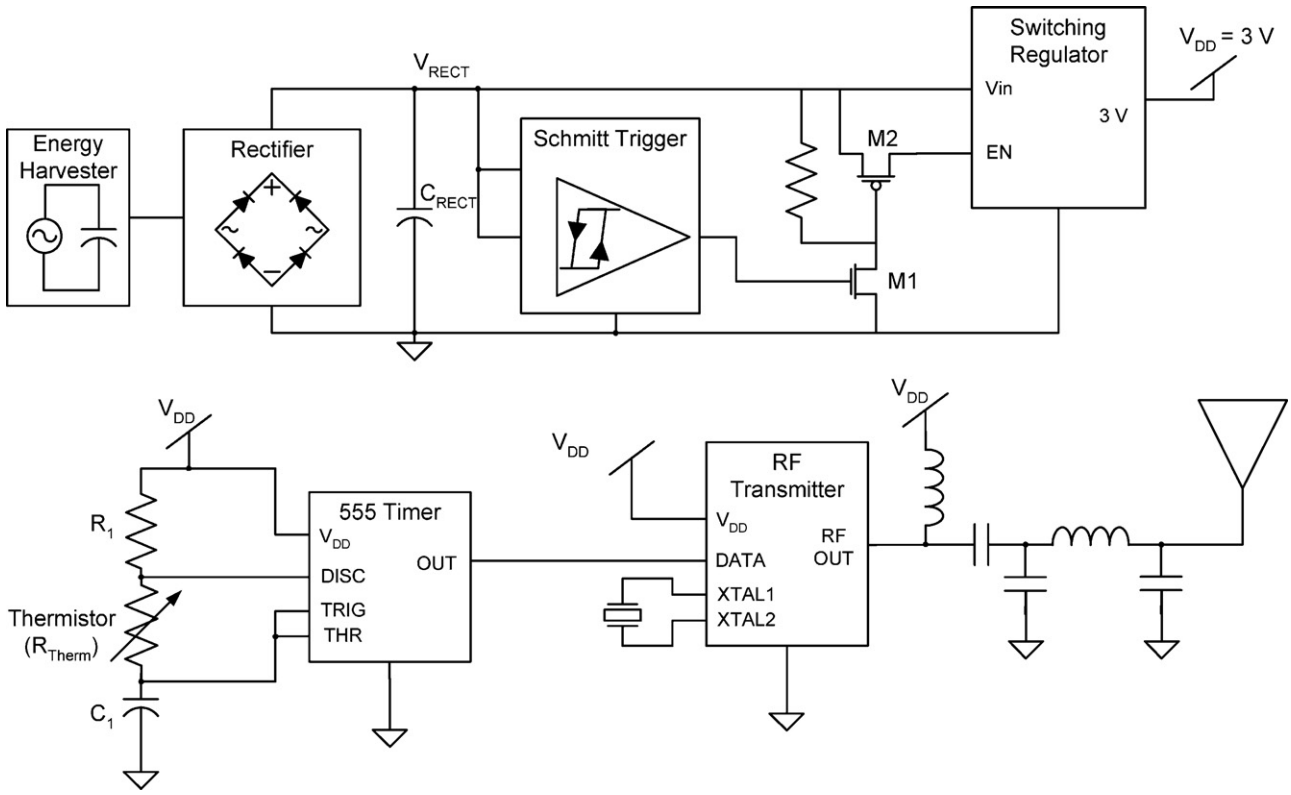

Fig. 7. Block diagram of sensor node circuitry.

less than half-power between the two peaks. The peak output powers for L_{CM} = 4 mm were 198 μW at 35 Hz and 184.9 μW at 41 Hz. The half-power frequencies are 34.4 and 42 Hz, giving a half-power bandwidth of 7.6 Hz and FBW of 19.9% (7.6/38.2). Thus, the FBW of the device with overhang mass is 4× the FBW of a typical single-mode device with FBW of 5%.

In energy harvesting, half-power bandwidth may not be the most appropriate definition, because the sensor electronics may be designed to operate below half-power. For example, if the sensor node circuitry and application only require 20 μW of power to operate, then the bandwidth using L_{CM} = 12 mm extends from 29.5 to 48 Hz, resulting in a FBW of 48%.

The measured and simulated results shown in Fig. 6 compare well when L_{CM} is large and the modes are relatively far apart. However, as the mode spacing decreases, the simulation results show a reduced power output. This is due to the fact that ANSYS does not correctly capture the displacement magnitude for small L_{CM}. Although the simulated displacement compares favorably to the measured one for L_{CM} = 9 mm and 12 mm, it becomes 3 times smaller when L_{CM} = 3 mm. The deviation between measurement and simulation is due to unmodeled boundary and continuity conditions in the finite element analysis, and material property variation. Nevertheless, good qualitative agreement and physically meaningful trends are obtained in the simulation for all cases.

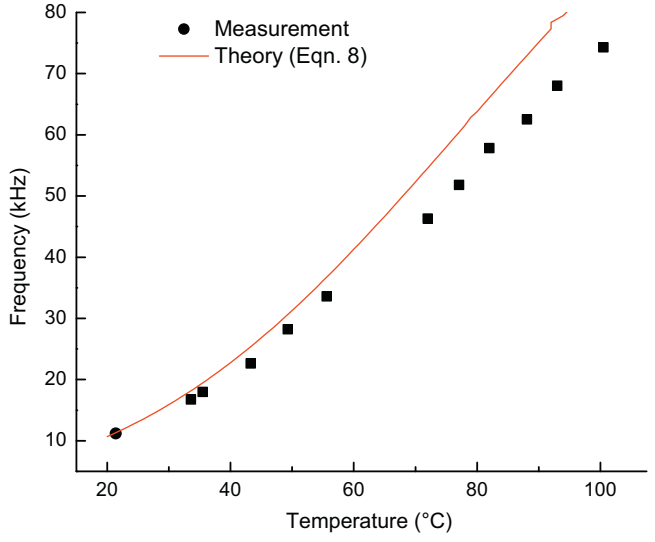

Fig. 8. Measured and theoretical sensor interface output frequency as a function of temperature.

3.3. Full system test

The energy harvester and circuit were tested together using the setup shown in Fig. 10 with a L_{CM} of 3 mm. The rectified voltage across the storage capacitor and the regulated voltage are shown in Fig. 11 at an energy harvester excitation frequency of 36.5 Hz. The rectifier storage capacitor with nominal value of 47 μF had a measured value of 38 μF. The storage capacitor voltage reaches the Schmitt trigger upper level of 6.2 V and turns on the transmitter until the voltage drops to 2.8 V. The lower threshold voltage is reduced compared to the designed value of 3.2 V, due to the large Schmitt trigger feedback resistors (several MΩ). The time that the regulator is enabled is 11.5 ms. Based on these numbers, the energy used per transmit cycle is 581 μJ [$0.5C_{Rect}(V_{high}^2 - V_{low}^2)$] and the power consumption during the transmit on time is 50.6 mW (581 μJ/11.5 ms), which is higher than the 37.6 mW measured in Section 3.1 due to the increased power consumption during startup. The time between transmissions at this operating condition is 3.44 s, meaning that it takes 3.44 s for the energy harvester to

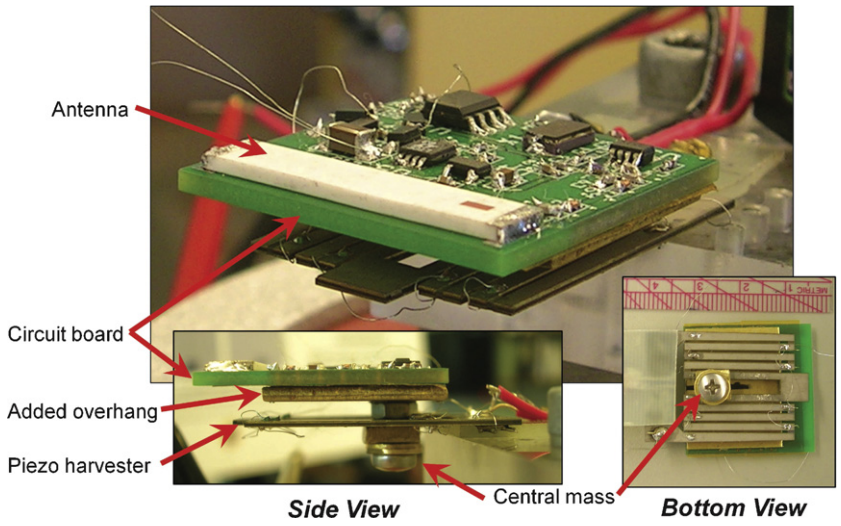

Fig. 9. Fabricated experimental device showing side and bottom view.

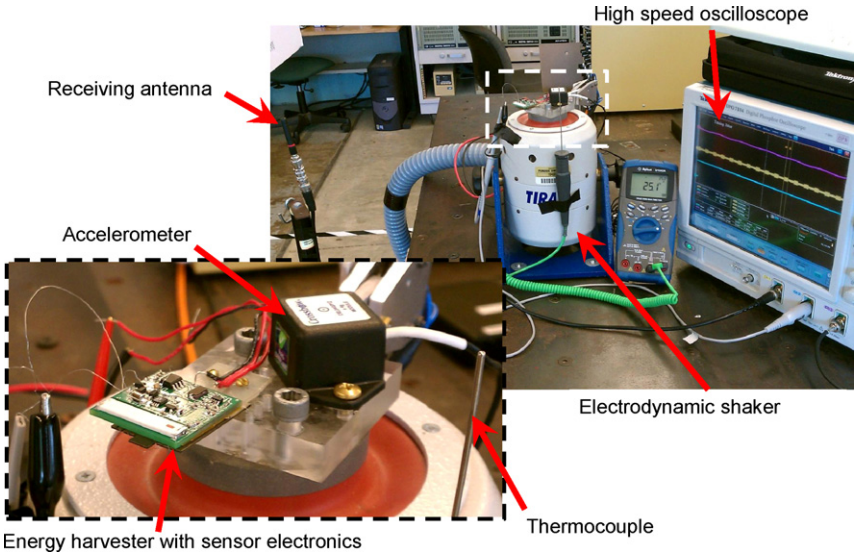

Fig. 10. Picture of experimental setup.

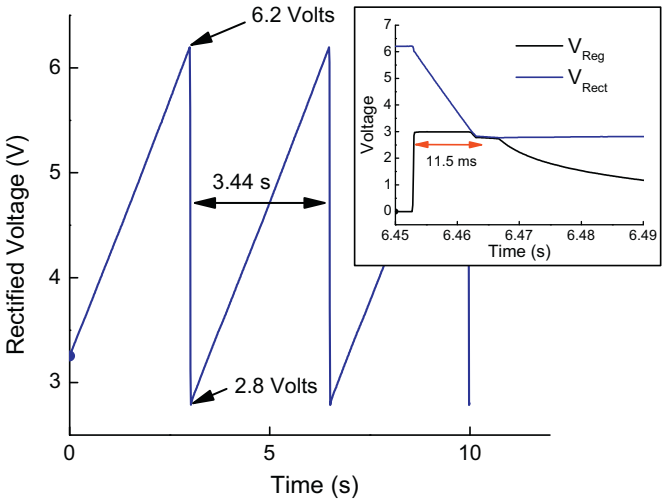

Fig. 11. Measured rectified voltage across storage capacitor and detailed view of rectified and regulated voltages during one transmission cycle.

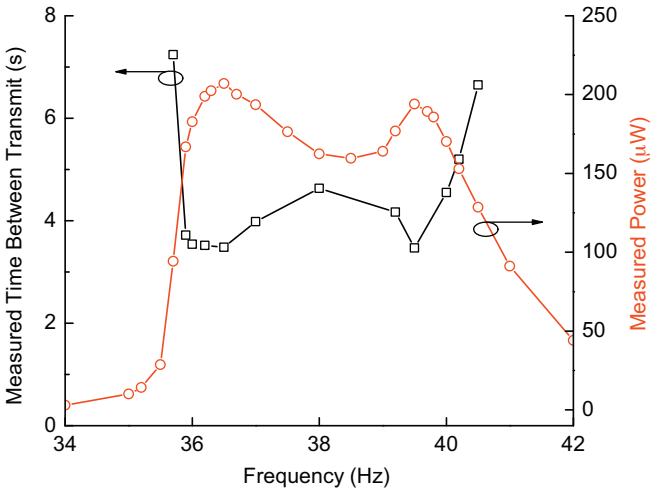

Fig. 12. Measured time between transmissions and measured AC power output for L_{CM} = 3 mm as a function of frequency.

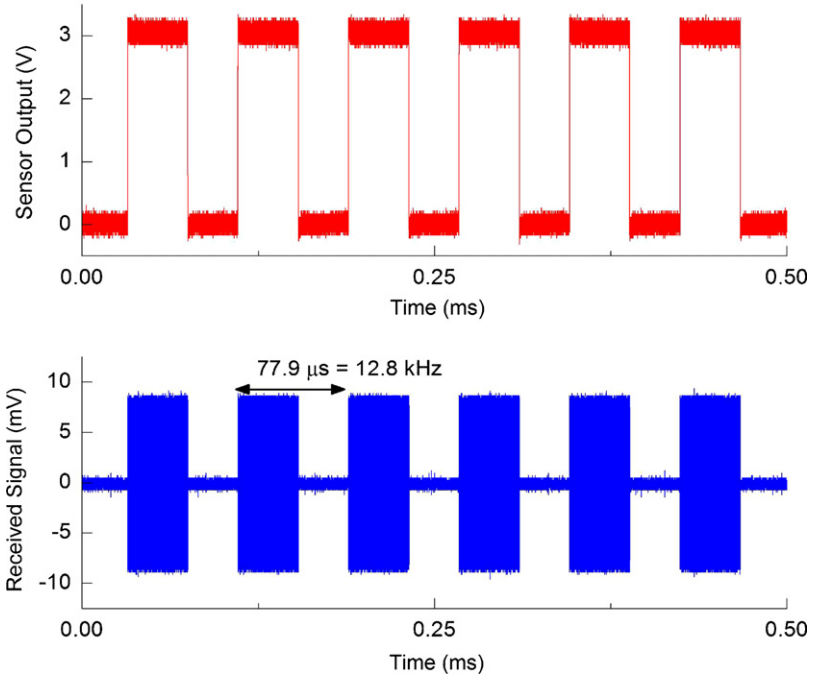

Fig. 13. Measured sensor interface output and received wireless signal.

replenish the energy used during transmission. Thus, the energy harvester harvests an average power of 169 μW (581 μJ/3.44 s), which is lower than the 207 μW measured in the stand alone energy harvester test as shown in Fig. 6 due to the loss in the rectifier and non-optimal load.

In the circuit of Fig. 7, the time between transmission cycles (as shown in Fig. 11) is a function of input power and therefore also a function of frequency. The measured RMS power output and time between transmissions is shown in Fig. 12 as a function of energy harvester excitation frequency at L_{CM} = 3 mm. This plot shows that when the energy harvester is at either one of the modal frequencies, the time between transmissions is shortest because the energy harvester has high power output and therefore can charge the energy reservoir capacitor more rapidly. As the excitation frequency deviates further from the peaks, the time between transmissions increases due to the reduced power.

The measured sensor interface output data and received wireless signal during the wireless test are shown in Fig. 13. The received wireless data's on–off keying clearly aligns well with the sensor interface output. The measured frequency of the OOK signal is 12.8 kHz. Based on interpolation from the measured sensor data in Fig. 8, the temperature corresponding to 12.8 kHz is 25.6 °C, which is a 2% error from the measured temperature of 25.1 °C measured by the thermocouple.

4. Conclusion

A sensor node powered by a wide bandwidth meandering vibration energy harvester with overhanging distributed mass has been developed. The energy harvester, for the first time, utilizes the electronics of the sensor node as a distributed inertial mass, resulting in a compact sensor node. The center frequency of the energy harvester is 38.2 Hz with a bandwidth of 7.6 Hz at L_{CM} = 4 mm, resulting in a fractional bandwidth of 19.9%, increasing the FBW by 4× over typical single-mode devices. This is believed to be the highest reported fractional bandwidth for a piezoelectric vibration energy harvester and the highest reported fractional bandwidth for an energy harvester operating at a low 0.2 g acceleration level. The power remains above 20 μW from 29.5 to 48 Hz, resulting in a 20-μW FBW of 48%. Peak output power at a vibration magnitude of 0.2 g for a central mass location of 4 mm was found to be 198 μW. The key developments in this work to enable an increased bandwidth were utilizing the sensor node electronics as an overhanging mass in combination with the meandering energy harvester's close spacing of natural frequencies. The entire system was demonstrated by using the energy harvester to completely power a 434 MHz wireless transmitter circuit to transmit temperature sensor data.

Acknowledgements

This work was partially supported by the Office of Naval Research (ONR) under the project entitled "Ultra Low-Size Self-Powered Wireless Sensors for Condition Monitoring of Cracks in Structural Components" and by the National Science Foundation (NSF) under CAREER Grant No. 074776. The authors would also like to thank Pornsak Srisungsitthisunti and Professor Xianfan Xu for their expertise in laser-machining the meandering energy harvester.

References

[1] H.A. Sodano, D.J. Inman, G. Park, A review of power harvesting from vibration using piezoelectric materials, Shock Vib. Dig. 36 (3) (2004) 197–205.
[2] R. Vullers, R. Schaijk, H. Visser, J. Penders, C. Hoof, Energy harvesting for autonomous wireless sensor networks, IEEE Solid-State Circuits Mag. 2 (2) (2010) 29–38.
[3] D. Zhu, S.P. Beeby, M.J. Tudor, N.R. Harris, A credit card sized self powered smart sensor node, Sens. Actuators A: Phys. 169 (2) (2011) 317–325.
[4] E. Sazonov, D. Curry, P. Pillay, Self-powered sensors for monitoring of highway bridges, IEEE Sens. J. 9 (11) (2009) 1422–1429.
[5] S.W. Arms, C.P. Townsend, D.L. Churchill, J.H. Galbreath, S.W. Mundell, Power management for energy harvesting wireless sensors, in: Proc. SPIE, vol. 5763, 2005, pp. 267–275.
[6] E.P. James, M.J. Tudor, S.P. Beeby, N.R. Harris, An investigation of self-powered systems for condition monitoring applications, Sens. Actuators A: Phys. 110 (1–3) (2004) 171–176.
[7] D. Zhu, M.J. Tudor, S.P. Beeby, Strategies for increasing the operating frequency range of vibration energy harvesters: a review, Meas. Sci. Technol. 21 (2) (2010) 1–29.

[8] S. Roundy, Y. Zhang, Toward self-tuning adaptive vibration-based microgenerators, in: Proc. SPIE, vol. 5649, 2005, pp. 373–384.
[9] C. Eichhorn, F. Goldschmidtboeing, P. Woias, Bidirectional frequency tuning of a piezoelectric energy converter based on a cantilever beam, J. Micromech. Microeng. 19 (9) (2009) 094006.
[10] T. Galchev, H. Kim, K. Najafi, Micro power generator for harvesting low-frequency and nonperiodic vibrations, IEEE J. MEMS 20 (4) (2011) 852–866.
[11] W. Li, T. Ho, G. Chan, P. Leong, Infrared signal transmission by a laser-micromachined, vibration-induced power generator, in: Proc. IEEE Midwest Symp. Circuits Syst., vol. 1, 2000, pp. 236–239.
[12] N. Ching, G. Chan, W. Li, H. Wong, P. Leong, PCB integrated micro-generator for wireless systems, in: Proc. Int. Symp. Smart Struct., vol. 1, Hong Kong, 2000.
[13] W.J. Li, Z. Wen, P.K. Wong, G.M. Chan, P.H.W. Leong, A micromachined vibration-induced power generator for low power sensors of robotic systems, in: World Autom. Congr. 8th Int. Symp. Robot. Appl., Maui, Hawaii, 2000.
[14] M. Elhami, M. El-Hami, P. Glynne-Jones, N. White, M. Hill, S. Beeby, E. James, A. Brown, J. Ross, Design and fabrication of a new vibration-based electromechanical power generator, Sens. Actuators A: Phys. 92 (1–3) (2001) 335–342.
[15] N. Ching, H. Wong, W. Li, P. Leong, Z. Wen, A laser-micromachined multi-modal resonating power transducer for wireless sensing systems, Sens. Actuators A: Phys. 97 (1–2) (2002) 685–690.
[16] N.N.H. Ching, H.Y. Wong, W.J. Li, P.H.W. Leong, Z. Wen, A laser-micromachined vibrational to electrical power transducer for wireless sensing systems, in: Proc. Int. Conf. Solid-State Sens. Actuators, June, Munich, Germany, 2001, pp. 1–4.
[17] J. Lee, S. Yuen, W. Li, P. Leong, Development of an AA size energy transducer with micro resonators, in: Proc. Int. Symp. Circuits Syst., vol. 4, Bangkok, Thailand, 1998, pp. IV-876–IV-879.
[18] P. Glynne-Jones, An electromagnetic, vibration-powered generator for intelligent sensor systems, Sens. Actuators A: Phys. 110 (1–3) (2004) 344–349.
[19] S. Beeby, M. Tudor, R. Torah, E. Koukharenko, Macro and micro scale electromagnetic kinetic energy harvesting generators, in: Proc. DTIP Conf., Stresa, Italy, 2006, pp. 26–28.
[20] S.P. Beeby, R.N. Torah, M.J. Tudor, P. Glynne-Jones, T. O'Donnell, C.R. Saha, S. Roy, A micro electromagnetic generator for vibration energy harvesting, J. Micromech. Microeng. 17 (7) (2007) 1257–1265.
[21] W. Huang, K. Tzeng, M. Cheng, R. Huang, A silicon MEMS micro power generator for wearable micro devices, J. Chin. Inst. Eng. 30 (1) (2007) 133–140.
[22] Perpetuum, Southampton, UK, PMG17 Data Sheet, 2010. URL: http://www.perpetuum.com/resources/PMG1720Datasheet.pdf.
[23] I. Ayala, D. Zhu, M. Tudor, Autonomous tunable energy harvester, in: Proc. PowerMEMS, Washington, DC, 2009, pp. 3–6.
[24] S.C. Chang, F.M. Yaul, A. Dominguez-Garcia, F. O'Sullivan, D.M. Otten, J.H. Lang, Harvesting energy from moth vibrations during flight, in: Proc. PowerMEMS, Washington, DC, 2009, pp. 57–60.
[25] E. Bouendeu, A. Greiner, P.J. Smith, J.G. Korvink, An efficient low cost electromagnetic vibration harvester, in: Proc. PowerMEMS, Washington, DC, 2009, pp. 320–323.
[26] P. Wang, X. Dai, X. Zhao, A micro electromagnetic vibration energy harvester with sandwiched structure and air channel for high energy conversion efficiency, in: Proc. PowerMEMS, Washington, DC, 2009, pp. 296–299.
[27] L. Wang, F.G. Yuan, Vibration energy harvesting by magnetostrictive material, Smart Mater. Struct. 17 (4) (2008) 045009.
[28] I. Sari, T. Balkan, H. Kulah, An electromagnetic micro power generator for wideband environmental vibrations, Sens. Actuators A: Phys. 145–146 (2008) 405–413.
[29] B.P. Mann, N.D. Sims, Energy harvesting from the nonlinear oscillations of magnetic levitation, J. Sound Vib. 319 (1–2) (2009) 515–530.
[30] S.J. Roundy, Energy scavenging for wireless sensor nodes with a focus on vibration to electricity conversion, Ph.D. thesis, The University of California, Berkeley, 2000.
[31] H. Fang, J. Liu, Z. Xu, L. Dong, L. Wang, D. Chen, B. Cai, Y. Liu, Fabrication and performance of MEMS-based piezoelectric power generator for vibration energy harvesting, Microelectron. J. 37 (11) (2006) 1280–1284.
[32] T.H. Ng, W.H. Liao, Sensitivity analysis and energy harvesting for a self-powered piezoelectric sensor, J. Intell. Mater. Syst. Struct. 16 (10) (2005) 785–797.
[33] V.R. Challa, M.G. Prasad, Y. Shi, F.T. Fisher, A vibration energy harvesting device with bidirectional resonance frequency tunability, Smart Mater. Struct. 17 (1) (2008) 015035.
[34] N.M. White, P. Glynne-Jones, S.P. Beeby, A novel thick-film piezoelectric micro-generator, Smart Mater. Struct. 10 (4) (2001) 850–852.
[35] M. Marzencki, Y. Ammar, S. Basrour, Integrated power harvesting system including a MEMS generator and a power management circuit, Sens. Actuators A: Phys. 145–146 (2008) 363–370.
[36] M. Zhu, E. Worthington, J. Njuguna, Analyses of power output of piezoelectric energy-harvesting devices directly connected to a load resistor using a coupled piezoelectric-circuit finite element method, IEEE Trans. Ultrason. Ferroelectr. Freq. Control 56 (7) (2009) 1309–1318.
[37] R. Elfrink, M. Renaud, T. Kamel, C. de Nooijer, S. Matova, R.V. Schaijk, Vacuum packaged MEMS piezoelectric vibration energy harvesters, in: Proc. PowerMEMS, Washington, DC, 2009, pp. 4–7.
[38] R. Elfrink, T.M. Kamel, M. Goedbloed, S. Matova, D. Hohlfeld, Y. van Andel, R. van Schaijk, Vibration energy harvesting with aluminum nitride-based piezoelectric devices, J. Micromech. Microeng. 19 (9) (2009) 094005.
[39] D.F. Berdy, P. Srisungsitthisunti, X. Xu, J. Rhoads, B. Jung, D. Peroulis, Compact low frequency meandered piezoelectric energy harvester, in: Proc. PowerMEMS, Washington, DC, 2009, pp. 71–74.
[40] J. Park, D. Lee, J. Park, Y. Chang, Y. Lee, High performance piezoelectric MEMS energy harvester based on D33 mode of PZT thin film on buffer-layer with PBTIO3 inter-layer, in: Proc. Int. Solid-State Sens. Actuators Microsyst. Conf. TRANSDUCERS, 2009, pp. 517–520.
[41] M. Renaud, P. Fiorini, R. van Schaijk, C. van Hoof, An impact based piezoelectric harvester adapted to low frequency environmental vibrations, in: Proc. Int. Solid-State Sens. Actuators Microsyst. Conf. TRANSDUCERS, 2009, pp. 2094–2097.
[42] M. Khbeis, J. McGee, R. Ghodssi, Development of a simplified hybrid ambient low frequency, low intensity vibration energy scavenger system, in: Proc. Int. Solid-State Sens. Actuators Microsyst. Conf. TRANSDUCERS, 2009, pp. 525–528.
[43] K. Adachi, T. Tanaka, An experimental power generation evaluation of cantilever type of piezoelectric vibration energy harvester, in: Proc. ASME Conf. Smart Mater. Adapt. Struct. Intell. Syst., 2009, pp. 281–289.
[44] E. Aktakka, R. Peterson, K. Najafi, Thinned-PZT on SOI process and design optimization for piezoelectric inertial energy harvesting, in: Proc. Int. Solid-State Sens. Actuators Microsyst. Conf. TRANSDUCERS, 2011, pp. 1649–1652.
[45] V. Bedekar, J. Oliver, S. Priya, Design and fabrication of bimorph transducer for optimal vibration energy harvesting, IEEE Trans. Ultrason. Ferroelectr. Freq. Control 57 (7) (2010) 1513–1523.
[46] A. Erturk, D.J. Inman, An experimentally validated bimorph cantilever model for piezoelectric energy harvesting from base excitations, Smart Mater. Struct. 18 (2) (2009) 025009.
[47] D. Guyomar, G. Sebald, H. Kuwano, Energy harvester of 1.5 cm^3 giving output power of 2.6 mW with only 1 g acceleration, J. Intell. Mater. Syst. Struct. 22 (5) (2010) 415–420.
[48] Y.K. Hong, K.S. Moon, Single crystal piezoelectric transducers to harvest vibration energy, in: Proc. SPIE, vol. 6048, SPIE, 2005, 60480E.
[49] H. Kim, V. Bedekar, R.A. Islam, W.-H. Lee, D. Leo, S. Priya, Laser-machined piezoelectric cantilevers for mechanical energy harvesting, IEEE Trans. Ultrason. Ferroelectr. Freq. Control 55 (9) (2008) 1900–1905.
[50] S.-L. Kok, N.M. White, N.R. Harris, Fabrication and characterization of free-standing thick-film piezoelectric cantilevers for energy harvesting, Meas. Sci. Technol. 20 (12) (2009) 124010.
[51] E.K. Reilly, L.M. Miller, R. Fain, P.K. Wright, A study of ambient vibrations for piezoelectric energy conversion, in: Proc. PowerMEMS, Washington, DC, 2009, pp. 312–315.
[52] D.F. Berdy, B. Jung, J.F. Rhoads, D. Peroulis, Increased-bandwidth, meandering vibration energy harvester, in: Proc. Int. Solid-State Sens. Actuators Microsyst. Conf. TRANSDUCERS, 2011, pp. 2638–2641.
[53] S. Priya, Advances in energy harvesting using low profile piezoelectric transducers, J. Electroceram. 19 (1) (2007) 167–184.
[54] T. Ning, F.-S. Wei, Multichannel coherence analysis of helicopter vibrations, in: Proc. Int. Conf. Signal Proc., vol. 2, 2002, pp. 1774–1777.
[55] A. Erturk, P.A. Tarazaga, J.R. Farmer, D.J. Inman, Effect of strain nodes and electrode configuration on piezoelectric energy harvesting from cantilevered beams, ASME J. Vibr. Acoust. 131 (1) (2009) 011010.
[56] M.A. Karami, D.J. Inman, Analytical modeling and experimental verification of the vibrations of the zigzag microstructure for energy harvesting, ASME J. Vibr. Acoust. 133 (1) (2011) 011002.
[57] Q. Wang, L. Cross, Constitutive equations of symmetrical triple layer piezoelectric benders, IEEE Trans. Ultrason. Ferroelectr. Freq. Control 46 (6) (1999) 1343–1351.
[58] S. Priya, D.J. Inman, Energy Harvesting Technologies, Springer, Boston, MA, 2009.
[59] IEEE Standard on Piezoelectricity, 1988.
[60] ANSYS Inc., ANSYS Release 13.0 Release Notes, 2010.
[61] S. Roundy, On the effectiveness of vibration-based energy harvesting, J. Intell. Mater. Syst. Struct. 16 (10) (2005) 809–823.
[62] Piezo Systems, Inc. website. URL: http://www.piezo.com/.
[63] M. Ferrari, V. Ferrari, M. Guizzetti, D. Marioli, An autonomous battery-less sensor module powered by piezoelectric energy harvesting with RF transmission of multiple measurement signals, Smart Mater. Struct. 18 (8) (2009) 085023.
[64] R. Torah, P. Glynne-Jones, M. Tudor, T. O'Donnell, S. Roy, S. Beeby, Self-powered autonomous wireless sensor node using vibration energy harvesting, Meas. Sci. Technol. 19 (12) (2008) 125202.
[65] Maxim Integrated Products, Sunnyvale, CA, USA, MAX1472 Data Sheet, 2010. http://datasheets.maxim-ic.com/en/ds/MAX1472.pdf.

Biographies

David F. Berdy received his B.S. degree in computer engineering from Rose-Hulman Institute of Technology, Terre Haute, IN, in 2008. He is currently pursuing his Ph.D. in electrical engineering in the School of Electrical and Computer Engineering at Purdue University, West Lafayette. His research interests include energy harvesting, MEMS transducers and their applications.

Byunghoo Jung received the B.S. degree from Yonsei University, Korea, in 1990, the M.S. degree from KAIST, Korea, in 1992, and the Ph.D. degree from the University of Minnesota, Twin Cities, in 2005. From 1992 to 1999, he was with Samsung Electronics, Korea, where he was involved in the design of video signal driver circuits for flat panel displays. Following receipt of his Ph.D. in January 2005, he was with Qualcomm in San Diego as a Senior RF IC Design Engineer until he joined the School of Electrical and Computer Engineering at Purdue University as an Assistant

Professor in August 2005. His research interests include analog, RF, and mixed-signal circuit design for wireless and wireline communications and bio-medical systems. He is the first place winner of the 2002–2003 SRC SiGe BiCMOS Design Challenge (as a lead designer) and the 2007–2008 SRC/SIA IC Design Challenge (as a lead faculty), and holds 10 US patents. He has been serving as a Co-Chair of the DAC/ISSCC Student Design Contest (SDC) since October 2006, as an Associate Editor of the IEEE Transactions on VLSI Systems since January 2009, and as a member of the Analog Signal Processing Technical Program Committee (ASPTPC) in the IEEE Circuits and System Society since May 2006.

Jeffrey F. Rhoads is an Assistant Professor in the School of Mechanical Engineering at Purdue University and is affiliated with both the Birck Nanotechnology Center and Ray W. Herrick Laboratories at the same institution. He received his B.S., M.S., and Ph.D. degrees, each in mechanical engineering, from Michigan State University in 2002, 2004, and 2007, respectively. Dr. Rhoads' current research interests include the predictive design, analysis, and implementation of resonant micro/nanoelectromechanical systems (MEMS/NEMS) for use in chemical and biological sensing, signal filtering, and inertial sensing systems, the behavior of nonlinear, parametrically excited systems and coupled oscillators, and the behavior of mechanical and/or electromechanical parametric amplifiers. Dr. Rhoads is a member of the American Society for Engineering Education (ASEE) and the American Society of Mechanical Engineers (ASME), where he serves on both the Student Design Committee and the Design Engineering Division's Technical Committee on Micro/Nanosystems. Dr. Rhoads is a 2009 recipient of the National Science Foundation's Faculty Early Career Development (CAREER) Award and the Purdue School of Mechanical Engineering's Harry L. Solberg Best Teacher Award.

Dimitrios Peroulis received his Ph.D. in Electrical Engineering from the University of Michigan at Ann Arbor in 2003. He has been with Purdue University since August 2003 where he is currently leading a group of graduate students on a variety of research projects in the areas of RF MEMS, sensing and power harvesting applications as well as RFID sensors for the health monitoring of sensitive equipment. He has been a PI or a co-PI in numerous projects funded by government agencies and industry in these areas. He is currently a key contributor in two DARPA projects at Purdue focusing on (1) very high quality ($Q > 1000$) RF tunable filters in mobile form factors (DARPA Analog Spectral Processing Program, Phases I, II and III) and on (2) developing comprehensive characterization methods and models for understanding the viscoelasticity/creep phenomena in high-power RF MEMS devices (DARPA M/NEMS S&T Fundamentals Program, Phases I and II). Furthermore, he is leading the experimental program on the Center for the Prediction of Reliability, Integrity and Survivability of Microsystems (PRISM) funded by the National Nuclear Security Administration. In addition, he is heading the development of the MEMS technology in a U.S. Navy project (Marines) funded under the Technology Insertion Program for Savings (TIPS) program focused on harsh-environment wireless micro-sensors for the health monitoring of aircraft engines. He has over 130 refereed journal and conference publications in the areas of microwave integrated circuits, sensors and antennas. He received the National Science Foundation CAREER award in 2008. His students have received numerous student paper awards and other student research-based scholarships. He is a Purdue University Faculty Scholar and has also received eight teaching awards including the 2010 HKN C. Holmes MacDonald Outstanding Teaching Award and the 2010 Charles B. Murphy award, which is Purdue University's highest undergraduate teaching honor.